# Physics-Informed Tensor Basis Neural Network for Turbulence Closure Modeling

**Leon Riccius, Atul Agrawal & Phaedon-Stelios Koutsourelakis**
Professorship of Data-driven Materials Modeling
School of Engineering and Design
Technical University of Munich
Boltzmannstr. 15, 85748 Garching, Germany
{leon.riccius, atul.agrawal, p.s.koutsourelakis}@tum.de

## Abstract

Despite the increasing availability of high-performance computational resources, Reynolds-Averaged Navier-Stokes (RANS) simulations remain the workhorse for the analysis of turbulent flows in real-world applications. Linear eddy viscosity models (LEVM), the most commonly employed model type, cannot accurately predict complex states of turbulence. This work combines a deep-neural-network-based, nonlinear eddy viscosity model with turbulence realizability constraints as an inductive bias in order to yield improved predictions of the anisotropy tensor. Using visualizations based on the barycentric map, we show that the proposed machine learning method's anisotropy tensor predictions offer a significant improvement over all LEVMs in traditionally challenging cases with surface curvature and flow separation. However, this improved anisotropy tensor does not, in general, yield improved mean-velocity and pressure field predictions in comparison with the best-performing LEVM.

## 1  Introduction

The incompressible Navier-Stokes equations are vital for describing fluid motion at low Reynolds numbers, impacting fields like aircraft design and ocean current modeling. Turbulent flows are prohibitively expensive to resolve fully, and engineers often resort to reduced models such as RANS for efficiency. These models employ closures such as the Launder-Sharma $k - \epsilon$ [1] or Wilcox's $k - \omega$ [2], which rely on linear assumptions, limiting their accuracy in complex flow scenarios. Nonlinear models have been explored but face challenges. This contribution builds upon the resurgence of turbulence modeling research, instigated by data-driven approaches [3], in response to the stagnation seen in the 2000s after earlier advancements.

This work combines additional flow features derived by Wang and colleagues [4, 5] with the neural network architecture proposed by Ling et al. [6] to give point-based estimates of the anisotropy tensor appearing in the RANS closure. The training objectives are supplemented by a loss term penalizing predictions that violate the physical realizability constraints of turbulent states. The trained network proposed was tested on unseen flow scenarios and used as a source term in the RANS equations to produce estimates of the mean-flow quantities.

| (a) Characteristic regions | (b) RANS $k - \omega$ | (c) DNS | (d) RGB mapping |
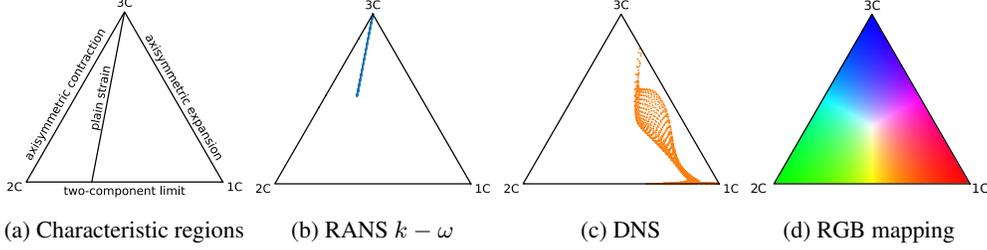
Figure 1: Barycentric map representing nature of turbulence of RANS $k - \omega$ **(a)** and DNS (b)

## 2 Physics-Informed Tensor Basis Neural Network

### 2.1 Reynolds stresses and realizability constraints

The Reynolds stress tensor $\tau_{ij} = \langle u_i u_j \rangle$, where $u_i = U_i - \langle U_i \rangle$ arises by time-averaging (mean indicated by $\langle \cdot \rangle$) of the Navier-Stokes equations and depends on the fluctuations $u_i$ of the velocity field $U_i$. It can be decomposed into an isotropic $\delta_{ij}$ and anisotropic $a_{ij}$ part which is given by $a_{ij} = \tau_{ij} - \frac{2}{3}k\delta_{ij}$. The turbulent kinetic energy $k$ is the trace of the Reynolds stresses.

The anisotropic $a_{ij}$ has zero trace, and its normalized version $b_{ij}$ is referred to as anisotropy tensor, i.e.:

$$b_{ij} = \frac{a_{ij}}{2k} = \frac{\tau_{ij}}{\langle u_k u_k \rangle} - \frac{1}{3}\delta_{ij}, \tag{1}$$

The Reynolds stress tensor is a symmetric, positive semi-definite second-order tensor with a non-negative determinant and trace. Following [7], the physical constraints, known also as realizability constraints, on the anisotropy tensor are:

$$-\frac{1}{3} \le b_{\alpha\alpha} \le \frac{2}{3} \quad \forall \alpha \in \{1, 2, 3\}, \qquad -\frac{1}{2} \le b_{\alpha\beta} \le \frac{1}{2} \quad \forall \alpha \ne \beta. \tag{2}$$

The barycentric map introduced in [8] uses an eigenvalue decomposition of $b$ to define three fundamental states of turbulence. All other states of turbulence can be expressed as a linear combination of these three limiting states. The limiting states form a triangle of all admissible states; its vertices are defined by the realizability constraints (2). As demonstrated in Figure 1, each point in the barycentric triangle corresponds to a unique color. The mapping is given in the supplementary material 6.1.

### 2.2 Closure Model

While LEVMs assume $b$ to be a linear function of the mean velocity gradient, a more general class of turbulence models can be formulated when dropping this assumption. The class of algebraic stress models is formed by nonlinear eddy viscosity models (NLEVM), which determine the Reynolds stresses from the local turbulent kinetic energy $k$, the eddy viscosity $\epsilon$, and the mean velocity gradient. Pope [9] has shown that every second-order tensor that can be formed from the normalized mean rate of strain $\hat{S} = \frac{\epsilon}{2k}(\nabla \langle U \rangle + \nabla \langle U \rangle^T)$ and the normalized rate of rotation $\hat{\Omega} = \frac{\epsilon}{2k}(\nabla \langle U \rangle - \nabla \langle U \rangle^T)$ and fulfills these requirements is a linear combination of ten basis tensors $\mathcal{T}_{ij}^{(n)}$. The most general form of a NLEVM is given by

$$b_{ij} = \sum_{n=1}^{10} G^{(n)}(\lambda_1, ...., \lambda_5) \, \mathcal{T}_{ij}^{(n)}(\hat{S}_{ij}, \hat{\Omega}_{ij}), \tag{3}$$

where $G^{(n)}$ are the coefficients of the basis tensors and $\lambda_k$ are the tensor invariants dependent on $\hat{S}$ and $\hat{\Omega}$. Ling et al. [6] introduced the Tensor Basis Neural Network (TBNN), which makes use of modern machine learning methods to learn these functions $G^{(n)}$ from high-fidelity fluid simulation data. Even though improved results compared to the $k - \epsilon$ model were reported, extracting enough information from these five invariants has proven difficult. This is especially true for flow cases with at least one direction of homogeneity, where invariants $\lambda_3$ and $\lambda_4$ vanish for the entire flow domain. Proof of this statement is given in the supplementary material 6.2. It is, however, possible to include

more features from local flow quantities and derive more invariants while still employing the integrity basis formed by $\mathcal{T}^{(n)}$. This work, in part, follows the research of Wang et al. [10], who derived an extended feature set also considering the gradients of the turbulent kinetic energy and the pressure. The model was implemented in PyTorch [11] and can be accessed via github.com/pkmtum/PI_TBNN.

### 2.2.1 Enforcing Realizability Constraints in Training

Ling et al. [6] enforced the realizability constraints in post-processing by simply projecting the points onto the closest boundary of the barycentric triangle. We propose incorporating these constraints in the TBNN's training, which we then colloquially refer to as the Physics-Informed Tensor Basis Neural Network (PI-TBNN). The inequalities given in Eq. (2) can be transformed into contributions to the loss function via the penalty method. The additional term reflects inductive bias about the problem structure and essentially acts as a regularizer. In plain words, if training samples are outside the domain of realizable turbulence states, the penalty term will force them back in. The constraints are

$$
\begin{aligned}
&c_1(\boldsymbol{b}) = \min_{\alpha}(b_{\alpha\alpha}) - 1/3 < 0 \quad \forall \alpha \in \{1,2,3\}, \quad && c_4(\boldsymbol{b}) = 2|b_{12}| - (b_{11} + b_{22} + 2/3) < 0, \\
&c_2(\boldsymbol{b}) = (3|\phi_2| - \phi_2)/2 - \phi_1 < 0, && c_5(\boldsymbol{b}) = 2|b_{13}| - (b_{11} + b_{33} + 2/3) < 0, \quad (4) \\
&c_3(\boldsymbol{b}) = 1/3 - \phi_2 < 0, && c_6(\boldsymbol{b}) = 2|b_{23}| - (b_{22} + b_{33} + 2/3) < 0,
\end{aligned}
$$

where $\phi_i$ denotes the eigenvalues of $\boldsymbol{b}$ in order to distinguish them from the invariants. $\phi_1$ and $\phi_2$ are the largest and second-largest eigenvalues. The penalty term is then given by

$$
\mathcal{L}(\hat{\boldsymbol{b}}(\boldsymbol{\lambda},\boldsymbol{\theta})) = \beta \sum_{k=1}^{6} \max(0, c_k(\hat{\boldsymbol{b}}(\boldsymbol{\lambda},\boldsymbol{\theta}))), \tag{5}
$$

where $\boldsymbol{\lambda}$ is the collection of invariants, $\boldsymbol{\theta}$ are the NN parameters, and $\hat{\boldsymbol{b}}(\boldsymbol{\lambda},\boldsymbol{\theta})$ is the predicted anisotropy tensor. The penalty coefficient $\beta$ determines its impact on the loss function. The complete loss function, considering the MSE loss, the regularization, and penalty terms, is given by

$$
E(\boldsymbol{\lambda}_i, \boldsymbol{\theta}) = \frac{1}{D} \sum_{i=1}^{D} \|\hat{\boldsymbol{b}}(\boldsymbol{\lambda}_i, \boldsymbol{\theta}) - \boldsymbol{b}_i\| + \frac{\alpha}{2}\|\boldsymbol{\theta}\|_2^2 + \frac{\beta}{D} \sum_{i=1}^{D} \sum_{k=1}^{6} \max(0, c_k(\hat{\boldsymbol{b}}(\boldsymbol{\lambda}_i, \boldsymbol{\theta}))), \tag{6}
$$

where $\boldsymbol{b}_i$ are the high-fidelity responses. The number of data points is denoted $D$. The coefficient $\alpha$ controls the degree of $L_2$ regularization.

## 3 Numerical Results

A total of four flow geometries were used as benchmarks in this work. The flow over periodic hills (PH) [12], the converging-diverging channel flow (CDC) [13], and the curved backward-facing step (CBFS) [14]. These exhibit adverse pressure gradients over curved surfaces, leading to flow separation and subsequent reattachment. The data set was also extended to include the square duct (SD) flow case [15]. This scenario clearly illustrates the limitations of LEVMs and is well-suited for investigating the forward propagation of the predicted anisotropy tensor. All flow cases were replicated in OpenFOAM [16] to obtain the baseline RANS data. The flow case setup is analogous to [17]. A detailed description of the data sets is given in the supplementary material 6.3.

### 3.1 Anisotropy Tensor Prediction

The PI-TBNN was tested on flow cases it had not seen during training. They differ either in geometry or Reynolds number from the training data. Figure 2 compares the anisotropy tensors for square duct (SD) using the barycentric colormap. Only the TBNN with the extended feature set can accurately reproduce the state of turbulence for this flow case. A similar picture arises on the PH geometry in Figure 3, where the $k - \omega$ model cannot capture 1C turbulence and axisymmetric expansion at the top and the bulk of the flow domain, respectively. The PI-TBNN, however, does exhibit such characteristics. For all test cases considered, the PI-TBNN achieves about 70% reduction of the RMSE compared to the baseline $k - \omega$ model and 50% reduction of the RMSE compared to [6] (see Table 1).
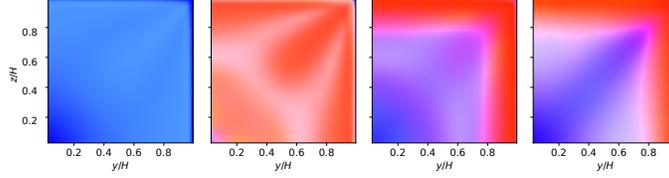
(a) LEVM $k-\omega$  (b) PI-TBNN1  (c) PI-TBNN2  (d) DNS

Figure 2: Stress types of $k-\omega$ **(a)**, PI-TBNN with FS1 **(b)**, FS[1-3] **(c)**, and DNS **(d)** for SD.

Table 1: RMSE of $b$ from RANS, PI-TBNN, and TBNN predictions for the three test cases.

| Flow case | LEVM $k-\omega$ | PI-TBNN, FS1 | PI-TBNN, FS[1-3] | TBNN Ling [6] |
|---|---|---|---|---|
| Square duct | 0.2175 | 0.0992 | 0.0663 | 0.14 |
| Periodic hills | 0.1016 | 0.0628 | 0.0419 | |
| Curved backward-facing step | 0.1173 | 0.0619 | 0.0414 | |

## 3.2 Anisotropy Tensor Propagation

While some applications involving wall shear stress computations may directly benefit from an improved prediction of $b$, the quantities of interest are usually the mean velocity and pressure fields. Hence, with the PI-TBNN model, the Reynolds equations were solved for the mean velocity and pressure fields. Table 2 shows that the PI-TBNN outperforms the $k-\epsilon$ model for the PH and CBFS geometries by a small margin and yields better in-plane prediction for the square duct flow case. The most accurate model, however, remains the $k-\omega$ model for all three test geometries. Surprisingly, on the CBFS geometry, the PI-TBNN shows the largest discrepancies in the region of the flow separation, as can be seen in Figure 4. The $k-\omega$ model even beats the mean field resulting from using the anisotropy tensor from the DNS on the periodic hills test case, indicating that an improved anisotropy tensor does not necessarily lead to improved mean velocity and pressure fields (behavior also reported in [18, 19]). Both [6] and [20] reported improvements in the mean-field prediction over a LEVM but used the $k-\epsilon$ as the baseline LEVM, which shows a larger discrepancy from the ground truth than the $k-\omega$ model, i.e. the best performing model of its class.

## 4 Conclusion

We introduced the PI-TBNN, which extended the TBNN framework with an extensive feature set and an inductive bias in the form of a physics-informed addition to the loss function. The addition of features was motivated both analytically—showing that the number of distinct invariants for 2D flow scenarios is three, not five—and empirically through improved predictions. It has been shown that the new approach yields more accurate predictions of the anisotropy tensor than the original TBNN of Ling et al. [6]. The improvements were illustrated with the barycentric colormap and quantified by comparing RMSEs. It is, however, limited in its predictive capabilities of the mean velocity and pressure fields. While it still outperformed the widely popular $k-\epsilon$ model on geometries with flow separation, it consistently fails to compete with the $k-\omega$ model. The rather large discrepancy of the RANS using the DNS anisotropy tensor indicates that it is more beneficial to train models that not only aim at improving predictions of the Reynolds stresses but instead target the mean field quantities directly, e.g., as in [21, 22, 23].
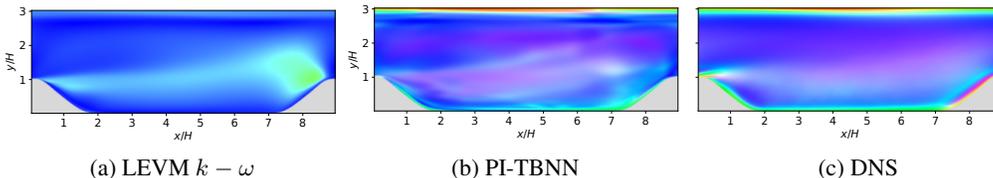


(a) LEVM $k-\omega$            (b) PI-TBNN            (c) DNS

Figure 3: Visualization of stress types of LEVM $k-\omega$ **(a)**, PI-TBNN **(b)**, and DNS **(c)**

4

Table 2: RMSE of $U$ for RANS with anisotropy tensor from $k - \omega$, $k - \epsilon$, PI-TBNN, and DNS. Reference velocity fields come from DNS.

| Flow case | $k - \omega$ | $k - \epsilon$ | $\boldsymbol{b}_{\mathrm{PI-TBNN}}$ | $\boldsymbol{b}_{\mathrm{DNS}}$ |
|---|---|---|---|---|
| Square duct RMSE($\boldsymbol{U}$) | 0.0496 | 0.0667 | 0.0716 | 0.0322 |
| Square duct RMSE($[U_2, U_3]$) | 0.0066 | 0.0066 | 0.0045 | 0.0025 |
| Periodic hills RMSE($\boldsymbol{U}$) | 0.0375 | 0.0545 | 0.0541 | 0.0465 |
| Curved backward-facing step RMSE($\boldsymbol{U}$) | 0.0609 | 0.0883 | 0.0868 | |



(a) Periodic hills



(b) Curved backward-facing step
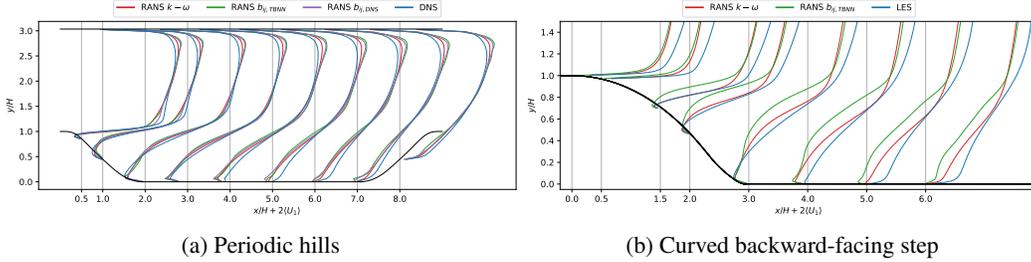
Figure 4: Streamwise mean velocity profiles at specific $x$-locations of PH **(a)**, and CBFS **(b)**.

## 5 Broader Impact

Turbulence is a key physical characteristic of a broad range of fluid flows. Understanding this phenomenon is crucial for complex designs, environmental modeling, and many more engineering applications. Computational power has increased massively in the past decades, enabling scale-resolving simulations like direct numerical simulations of a number of canonical turbulent flows. However, fast approximations like the RANS continue to remain essential for industrial applications, whose accuracy hinges heavily on turbulence closure models.

The presented research serves as an extension to the state-of-the-art data-driven turbulence closure model proposed by [6]. By combining a deep neural network with an inductive bias informed by turbulence realizability constraints, plus an extensive feature set, the PI-TBNN showed considerable improvements. These improvements showcased through barycentric colormap visualizations and quantified reductions in RMSE signify a step forward in our ability to capture complex turbulence states, particularly in scenarios involving surface curvature and flow separation.

However, the study also sheds light on the nuanced relationship between improved anisotropy tensor predictions and the ultimate goal of predicting mean velocity and pressure fields. While the PI-TBNN excels in enhancing anisotropy tensor predictions, it does not consistently outperform the established $k - \omega$ model in mean-field predictions, underscoring the need for further exploration in this area.

We do not see any direct ethical concerns associated with this research. The impact on society is primarily through the over-arching context of research using machine learning to improve our general understanding of turbulence in fluids.

# References

[1] B. E. Launder and B. I. Sharma. "Application of the energy-dissipation model of turbulence to the calculation of flow near a spinning disc". In: *Letters in Heat and Mass Transfer* 1.2 (Nov. 1974), pp. 131–137. ISSN: 00944548. DOI: 10.1016/0094-4548(74)90150-7.

[2] David C. Wilcox. "Formulation of the k-$\omega$ turbulence model revisited". In: *AIAA Journal*. Vol. 46. 11. Nov. 2008, pp. 2823–2838. DOI: 10.2514/1.36541. URL: https://arc.aiaa.org/doi/abs/10.2514/1.36541.

[3] Karthik Duraisamy, Gianluca Iaccarino, and Heng Xiao. "Turbulence Modeling in the Age of Data". In: *Annual Review of Fluid Mechanics* 51.1 (2019), pp. 357–377. ISSN: 0066-4189. DOI: 10.1146/annurev-fluid-010518-040547.

[4] Jian Xun Wang and Heng Xiao. "Data-driven CFD modeling of turbulent flows through complex structures". In: *International Journal of Heat and Fluid Flow* 62 (2016), pp. 138–149. ISSN: 0142727X. DOI: 10.1016/j.ijheatfluidflow.2016.11.007.

[5] Jian Xun Wang, Jin Long Wu, and Heng Xiao. "Physics-informed machine learning approach for reconstructing Reynolds stress modeling discrepancies based on DNS data". In: *Physical Review Fluids* 2.3 (2017), p. 34603. ISSN: 2469990X. DOI: 10.1103/PhysRevFluids.2.034603.

[6] Julia Ling, Andrew Kurzawski, and Jeremy Templeton. "Reynolds averaged turbulence modelling using deep neural networks with embedded invariance". In: *Journal of Fluid Mechanics* 807 (2016), pp. 155–166. ISSN: 14697645. DOI: 10.1017/jfm.2016.615.

[7] U. Schumann. "Realizability of Reynolds-stress turbulence models". In: *Physics of Fluids* 20.5 (1977), pp. 721–725. ISSN: 10706631. DOI: 10.1063/1.861942. URL: https://doi.org/10.1063/1.861942.

[8] S. Banerjee et al. "Presentation of anisotropy properties of turbulence, invariants versus eigenvalue approaches". In: *Journal of Turbulence* 8 (2007), pp. 1–27. ISSN: 14685248. DOI: 10.1080/14685240701506896. URL: https://www-tandfonline-com.eaccess.ub.tum.de/doi/abs/10.1080/14685240701506896.

[9] S. B. Pope. "A more general effective-viscosity hypothesis". In: *Journal of Fluid Mechanics* 72.2 (Nov. 1975), pp. 331–340. ISSN: 14697645. DOI: 10.1017/S0022112075003382. URL: http://www.journals.cambridge.org/abstract_S0022112075003382.

[10] Jian Xun Wang et al. *A comprehensive physics-informed machine learning framework for predictive turbulence modeling*. 2017. DOI: 10.1103/PhysRevFluids.3.074602.

[11] Adam Paszke et al. *PyTorch: An imperative style, high-performance deep learning library*. Dec. 2019. URL: http://arxiv.org/abs/1912.01703.

[12] C P Mellen, J Frohlic, and W. Rodi. "Large Eddy Simulation of the flow over periodic hills". In: *16th IMACS World Congress* (2000), pp. 3–8.

[13] Jean Philippe Laval and Matthieu Marquillie. "Direct numerical simulations of converging–diverging channel flow". In: *ERCOFTAC Series*. Vol. 14. Springer Netherland, 2011, pp. 203–209. ISBN: 9789048196029. DOI: 10.1007/978-90-481-9603-6{\_}21.

[14] Yacine Bentaleb, Sylvain Lardeau, and Michael A. Leschziner. "Large-eddy simulation of turbulent boundary layer separation from a rounded step". In: *Journal of Turbulence* 13 (Jan. 2012), pp. 1–28. ISSN: 14685248. DOI: 10.1080/14685248.2011.637923. URL: https://www.tandfonline.com/doi/full/10.1080/14685248.2011.637923.

[15] Alfredo Pinelli et al. "Reynolds number dependence of mean flow structure in square duct turbulence". In: *Journal of Fluid Mechanics* 644 (2010), pp. 107–122. ISSN: 00221120. DOI: 10.1017/S0022112009992242. URL: http://openaccess.city.ac.uk/.

[16] H. G. Weller et al. "A tensorial approach to computational continuum mechanics using object-oriented techniques". In: *Computers in Physics* 12.6 (Dec. 1998), p. 620. ISSN: 08941866. DOI: 10.1063/1.168744. URL: http://scitation.aip.org/content/aip/journal/cip/12/6/10.1063/1.168744.

[17] Leon Riccius. *Machine Learning Augmented Turbulence Modelling for the Reynolds Stress Closure Problem*. Munich, Mar. 2021.

[18] Salar Taghizadeh, Freddie D. Witherden, and Sharath S. Girimaji. "Turbulence closure modeling with data-driven techniques: physical compatibility and consistency considerations". In: *New Journal of Physics* 22.9 (Sept. 2020), p. 093023. ISSN: 1367-2630. DOI: 10.1088/1367-2630/ABADB3. URL: https://iopscience.iop.org/article/10.1088/1367-2630/abadb3%20https://iopscience.iop.org/article/10.1088/1367-2630/abadb3/meta.

[19] Karthik Duraisamy. "Perspectives on machine learning-augmented Reynolds-averaged and large eddy simulation models of turbulence". In: *Physical Review Fluids* 6.5 (May 2021), p. 050504. ISSN: 2469990X. DOI: 10.1103/PHYSREVFLUIDS.6.050504/FIGURES/5/MEDIUM. URL: https://journals.aps.org/prfluids/abstract/10.1103/PhysRevFluids.6.050504.

[20] Jin Long Wu, Heng Xiao, and Eric Paterson. "Physics-informed machine learning approach for augmenting turbulence models: A comprehensive framework". In: *Physical Review Fluids* 7.3 (2018), p. 74602. ISSN: 2469990X. DOI: 10.1103/PhysRevFluids.3.074602.

[21] Atul Agrawal and Phaedon-Stelios Koutsourelakis. "A probabilistic, data-driven closure model for RANS simulations with aleatoric, model uncertainty". In: *arXiv preprint* (July 2023). DOI: https://doi.org/10.48550/arXiv.2307.02432. URL: http://arxiv.org/abs/2307.02432.

[22] Michael E. Hayek, Qiqi Wang, and Gregory M. Laskowski. "Adjoint-based optimization of RANS eddy viscosity model for U-bend channel flow". In: *AIAA Aerospace Sciences Meeting, 2018*. 210059. Reston, Virginia: American Institute of Aeronautics and Astronautics Inc, AIAA, Jan. 2018. ISBN: 9781624105241. DOI: 10.2514/6.2018-2091. URL: https://arc.aiaa.org/doi/10.2514/6.2018-2091.

[23] Eric J Parish and Karthik Duraisamy. "A paradigm for data-driven predictive modeling using field inversion and machine learning". In: *Journal of Computational Physics* 305 (2016), pp. 758–774. ISSN: 10902716. DOI: 10.1016/j.jcp.2015.11.012. URL: http://www.elsevier.com/open-access/userlicense/1.0/.

# 6 Supplementary Material

## 6.1 RGB colormap

As demonstrated in Figure 1, each point in the barycentric triangle corresponds to a unique color. The mapping from the barycentric coordinates to the RGB values follows

$$\begin{bmatrix} R \\ G \\ B \end{bmatrix} = \frac{1}{\max C_{ic}} \left( C_{1c} \begin{bmatrix} 1 \\ 0 \\ 0 \end{bmatrix} + C_{2c} \begin{bmatrix} 0 \\ 1 \\ 0 \end{bmatrix} + C_{3c} \begin{bmatrix} 0 \\ 0 \\ 1 \end{bmatrix} \right) \quad \text{for } i \in \{1, 2, 3\}. \tag{7}$$

## 6.2 Scalar invariants

Two of the five scalar invariants $(\lambda_3, \lambda_4)$ are zero for flows with one direction of homogeneity. The two invariants read

$$\lambda_3 = \text{tr}(\hat{\boldsymbol{S}}^3), \qquad\qquad \lambda_4 = \text{tr}(\hat{\boldsymbol{\Omega}}^2 \hat{\boldsymbol{S}}). \tag{8}$$

Assuming the flow is homogeneous in $z$-direction, the partial derivatives of the mean velocity with respect to $z$ vanish, and the mean rate of strain and rotation read

$$\hat{S}_{ij} = \frac{1}{2}\frac{k}{\epsilon} \begin{bmatrix} 2\frac{\partial \langle U_x \rangle}{\partial x} & \frac{\partial \langle U_x \rangle}{\partial y} + \frac{\partial \langle U_y \rangle}{\partial x} \\ \frac{\partial \langle U_y \rangle}{\partial x} + \frac{\partial \langle U_x \rangle}{\partial y} & 2\frac{\partial \langle U_y \rangle}{\partial y} \end{bmatrix}, \quad \hat{\Omega}_{ij} = \frac{1}{2}\frac{k}{\epsilon} \begin{bmatrix} 0 & \frac{\partial \langle U_x \rangle}{\partial y} - \frac{\partial \langle U_y \rangle}{\partial x} \\ \frac{\partial \langle U_y \rangle}{\partial x} - \frac{\partial \langle U_x \rangle}{\partial y} & 0 \end{bmatrix}. \tag{9}$$

The incompressibility constraint of the Reynolds equations reduces to

$$\frac{\partial \langle U_i \rangle}{\partial x_i} = \text{tr}\left( \frac{\partial \langle U_i \rangle}{\partial x_j} \right) = \frac{\partial \langle U_x \rangle}{\partial x} + \frac{\partial \langle U_y \rangle}{\partial y} = 0. \tag{10}$$

When using the simplified expressions of $\hat{\boldsymbol{S}}$ and $\hat{\boldsymbol{\Omega}}$ in combination with the incompressibility constraint, invariant $\lambda_3$ is given by

$$\text{tr}(\hat{S}_{ij}^3) = \tag{11}$$

$$\frac{k^3}{8\epsilon^3}\text{tr}\left(\begin{bmatrix} \hat{S}_{11}(\hat{S}_{11}^2 + \hat{S}_{12}^2) + \hat{S}_{12}(\hat{S}_{11}\hat{S}_{12} + \hat{S}_{12}\hat{S}_{22}) & \hat{S}_{12}(\hat{S}_{11}^2 + \hat{S}_{12}^2) + \hat{S}_{22}(\hat{S}_{11}\hat{S}_{12} + \hat{S}_{12}\hat{S}_{22}) \\ \hat{S}_{11}(\hat{S}_{11}\hat{S}_{12} + \hat{S}_{12}\hat{S}_{22}) + \hat{S}_{12}(\hat{S}_{12}^2 + \hat{S}_{22}^2) & \hat{S}_{22}(\hat{S}_{12}^2 + \hat{S}_{22}^2) + \hat{S}_{12}(\hat{S}_{11}\hat{S}_{12} + \hat{S}_{12}\hat{S}_{22}) \end{bmatrix}\right)$$

$$= \frac{k^3}{8\epsilon^3}\left(\hat{S}_{11}(\hat{S}_{11}^2 + \hat{S}_{12}^2) + 2\hat{S}_{12}^2\underbrace{(\hat{S}_{11} + \hat{S}_{22})}_{=0} + \hat{S}_{22}(\hat{S}_{22}^2 + \hat{S}_{12}^2)\right), \tag{12}$$

$$= \frac{k^3}{8\epsilon^3}\left(\hat{S}_{11}(\hat{S}_{11}^2 + \hat{S}_{12}^2) + \hat{S}_{22}(\hat{S}_{11}^2 + \hat{S}_{12}^2)\right), \tag{13}$$

$$= \frac{k^3}{8\epsilon^3}\left(\underbrace{(\hat{S}_{11} + \hat{S}_{22})}_{=0}(\hat{S}_{11}^2 + \hat{S}_{12}^2)\right) = 0. \tag{14}$$

The derivation of invariant $\lambda_4$ is more straightforward and thus written in terms of the mean velocity gradient. It is given by

$$\text{tr}(\hat{\Omega}_{ij}^2\hat{S}_{jk}) = \text{tr}\left(\frac{k^3}{8\epsilon^3}\left(\frac{\partial\langle U_x\rangle}{\partial y} - \frac{\partial\langle U_y\rangle}{\partial x}\right)^2\begin{bmatrix} 2\frac{\partial\langle U_x\rangle}{\partial x} & \frac{\partial\langle U_x\rangle}{\partial y} + \frac{\partial\langle U_y\rangle}{\partial x} & 0 \\ \frac{\partial\langle U_y\rangle}{\partial x} + \frac{\partial\langle U_x\rangle}{\partial y} & 2\frac{\partial\langle U_y\rangle}{\partial y} & 0 \\ 0 & 0 & 0 \end{bmatrix}\right) \tag{15}$$

$$= \frac{k^3}{4\epsilon^3}\left(\frac{\partial\langle U_x\rangle}{\partial y} - \frac{\partial\langle U_y\rangle}{\partial x}\right)\underbrace{\left(\frac{\partial\langle U_x\rangle}{\partial x} + \frac{\partial\langle U_y\rangle}{\partial y}\right)}_{=0} = 0. \tag{16}$$

### 6.3 Data set

The high-fidelity direct numerical simulation (DNS)/large eddy simulation (LES) data are used for the training. Out of the two available DNS for the CDC, the one at $\text{Re} = 7900$ was used for estimating the regularization parameters. The higher Reynolds number simulation at $\text{Re} = 12600$ was used for training and validation, along with the DNS at $\text{Re} = 2800$ and LES at $\text{Re} = 10595$ for PH and the DNS for SD at $\text{Re} = \{2000, 2400, 2900, 3200\}$. The data set was split into training and validation sets at a ratio of $70/30$. Therefore, the total number of data points available for training was 26600.

The testing set consists of three flow geometries (SD, PH, and CBFS). Two of these geometries, SD and PH, are also part of the training and validation set, however, at different Reynolds numbers. The periodic hills case at $\text{Re} = 5600$ was selected to investigate the interpolation properties — the ML model has previously seen this flow geometry and is expected to yield good predictions. The square duct is a canonical flow case that clearly illustrates the deficiencies of the LEVMs and is suitable to present difficulties of propagating the Reynolds stresses to the flow field. Finally, the curved backward-facing step tests the ML model's extrapolation capabilities.